Research Article

Assessment of *Kaistella jeonii* esterase conformational dynamics in response to poly(ethylene terephthalate) binding

Ederson Sales Moreira Pinto [a], Arthur Tonietto Mangini [a], Lorenzo Chaves Costa Novo [a], Fernando Guimaraes Cavatao [a], Mathias J. Krause [d], Marcio Dorn [a,b,c,*]

[a] *Center for Biotechnology, Federal University of Rio Grande do Sul, Av. Bento Gonçalves, 9500, Buildings 43421, Porto Alegre, RS, Brazil*
[b] *Institute of Informatics, Federal University of Rio Grande do Sul, Av. Bento Gonçalves, 9500, Building 43424, Porto Alegre, RS, Brazil*
[c] *National Institute of Science and Technology - Forensic Science, Porto Alegre, RS, Brazil*
[d] *Institute for Applied and Numerical Mathematics, Karlsruhe Institute of Technology, Englerstraße 2, D-76131, Karlsruhe, BW, Germany*

ARTICLE INFO

ABSTRACT

The pervasive presence of plastic in the environment has reached a concerning scale, being identified in many ecosystems. Bioremediation is the cheapest and most eco-friendly alternative to remove this polymer from affected areas. Recent work described that a novel cold-active esterase enzyme extracted from the bacteria *Kaistella jeonii* could promiscuously degrade PET. Compared to the well-known PETase from *Ideonella sakaiensis*, this novel esterase presents a low sequence identity yet has a remarkably similar folding. However, enzymatic assays demonstrated a lower catalytic efficiency. In this work, we employed a strict computational approach to investigate the binding mechanism between the esterase and PET. Understanding the underlying mechanism of binding can shed light on the evolutive mechanism of how enzymes have been evolving to degrade these artificial molecules and help develop rational engineering approaches to improve PETase-like enzymes. Our results indicate that this esterase misses a disulfide bridge, keeping the catalytic residues closer and possibly influencing its catalytic efficiency. Moreover, we describe the structural response to the interaction between enzyme and PET, indicating local and global effects. Our results aid in deepening the knowledge behind the mechanism of biological catalysis of PET degradation and as a base for the engineering of novel PETases.

1. Introduction

Plastic pollution is not only an emergent threat to human health and biodiversity but is nearing an irreversible point (MacLeod et al., 2021). Plastic residues are found globally in food, water, and in almost every ecosystem (Carr et al., 2016; Revel et al., 2018; Allouzi et al., 2021; MacLeod et al., 2021; Howard and McCarthy, 2023). Remarkably, poly(ethylene terephthalate) (PET)-based plastics are one of the most used in packaging industries because of their durability (Maurya et al., 2020). Amidst the mass-produced plastic, recycling only takes place for a diminutive share (Howard and McCarthy, 2023). The remaining plastic reaches the environment and negatively impacts its surroundings and diverse life forms (Maurya et al., 2020). In response to the challenges of plastic pollution, cost-effective and eco-friendly bioremediation is gaining prominence (Sharma et al., 2018). Ongoing

advancements in microbial enzymes, genetic engineering, and enzyme immobilization emphasize the potential of enzymatic remediation in this field (Sharma et al., 2018). Currently, cutinases are the main enzymes used for plastic degradation (Egmond and de Vlieg, 2000; Maurya et al., 2020).

In 2016, Yoshida et al. (2016) described that *Ideonella sakaiensis* could degrade PET. The characterization of the enzyme *Is*PETase enabled several studies for protein engineering (Son et al., 2019; Cui et al., 2021) and, until now, is one of the most effective enzymes for PET degradation. Simulations using Molecular Dynamics (MD) were conducted to understand and optimize the *Is*PETase activity (Fecker et al., 2018; Chen et al., 2021), giving more information about enzyme characteristics crucial for protein engineering. MD gives atomistic information about the dynamic molecular mechanism that determines the protein stability, function, and protein-ligand interaction and is a reliable strat-

Fig. 1. A) Structure of the esterase (PET30), highlighting the disulfide bridge formed by residues Cys262 and Cys285, and the catalytic residues Ser153, Asp198, and His230. B) Chemical formula representing PET monomer and PETase degradation products, MHET and BHET. C) Schematics of the general reaction mechanism of esterases, depicting the expected reaction of the esterase's catalytic triad.

egy to access a protein's molecular behavior (Childers and Daggett, 2017). Therefore, using MD can provide substantial data for enzyme management in bioremediation.

In 2022, a new esterase was described from *Kaistella jeonii* (PET30) that showed PET degradation activity (Zhang et al., 2022). PET30 **Fig. 1**A, classified as an esterase (serine protease) with EC 3.1 designation, represents a hydrolase acting specifically on ester bonds. Enzymes denoted as "PETases" can degrade PET by cleaving the ester bonds of the polymer into Mono-2-hydroxyethyl terephthalate (MHET) and Bis(2-hydroxyethyl) terephthalate (BHET) **Fig. 1**B. In alignment with this enzymatic function, PET30 likely falls under the EC sub-subtype 1 (EC 3.1.1), akin to cutinases, lipases, and carboxylesterases known for their PETase activity. Positioned within the α/β hydrolase superfamily, alongside enzymes like lipases and esterases, PET30 features a distinctive Gly – x1 – Ser – x2 – Gly motif (Gly151 – Trp152 – Ser153 – Met154 – Gly155) at its active site. Strikingly, this motif mirrors the identical sequence found in *Is*PETase (Gly158 – Trp159 – Ser160 – Met161 – Gly162), further underlining the structural similarity between these PET-degrading enzymes (Joo et al., 2018).

A notable feature of PET30 is its catalytic triad, a defining characteristic of α/β hydrolases. Comprising the residues Asp-His-Ser **Fig. 1**C, this triad underscores PET30's enzymatic functionality. When aligned with *Is*PETase structure, PET30 reveals a less hydrophobic environment surrounding its catalytic pocket, providing an initial distinction between these structurally akin enzymes.

Despite a relatively low sequence identity of 34% with *Is*PETase, PET30's tertiary structure mirrors its PET-degrading counterpart. Displaying a canonical α/β-fold, PET30 features a central twisted β-sheet comprising ten β-strands, flanked by seven α-helices on either side - a structural arrangement similar to *Is*PETase (Zhang et al., 2022).

In this work, noting the performance of PET degradation and some common characteristics with *Is*PETase, we observe the potential use of this new esterase on the bioremediation of PET. Furthermore, the report of the enzyme's molecular mechanism could give more information on

cutinase's evolutionary pathway toward PET degradation. Therefore, we use a classic MD to understand and compare the protein's molecular behavior with the *Is*PETase literature available.

2. Methodology

2.1. Protein structure, modeling, and validation

We retrieved the initial structure of PET30 from the Protein Data Bank (PDB) under the identifier 7PZJ (Berman et al., 2000). Due to the absence of the initial segment (residues 1-27), a comparative modeling approach was employed. The structure was subjected to the Robetta server (Kim et al., 2004) for structure modeling and refinement. The resultant model comprises residues 1 to 299, integrating the reconstructed N-terminal segment. The accuracy and reliability of the generated model were assessed through various validation tools (Bowie et al., 1991; Lüthy et al., 1992; Colovos and Yeates, 1993; Laskowski et al., 1993; Hooft et al., 1996; Pontius et al., 1996; Williams et al., 2018) to ensure its suitability for subsequent analyses.

2.2. Ensemble docking and initial simulation

The molecular structure of PET was modeled using Marvin JS (Csizmadia, 1999) in a trimer format. Next, we submitted the structure to the LigParGen server (Jorgensen and Tirado-Rives, 2005; Dodda et al., 2017a,b), which generates parameters for bonds, angles, dihedrals, and Lennard-Jones interactions for the selected forcefield (FF). We use the 1.14*CM1A option for partial charge parameters. The server also provided topology files compatible with GROMACS for further simulations.

We employed AutoDock Tools 1.5.7 (Sanner et al., 1999) and AutoDock Vina 1.2.3 (Trott and Olson, 2010; Eberhardt et al., 2021) software for molecular docking of the PET molecule into the esterase structure. A grid box was strategically positioned at the central coordinates of the catalytic residues, namely Ser153, Asp198, and His230.

To mimic the native state of the residues, we protonated the nitrogen δ of His230 while concurrently deprotonating the nitrogen ϵ. The dimensions of the grid box were set to encompass the entire active enzyme center, with a grid size of 26 Å on the x-axis, 21.5 Å on the y-axis, and 16.3 Å on the z-axis. Subsequently, we imported the ligand into AutoDock Vina, which generated ten different poses. The resultant conformation of the ligand, as generated by AutoDock Vina, was employed in subsequent molecular dynamics simulations.

We conducted Molecular Dynamics (MD) simulations using the GROMACS package version 2021.5 (Lindahl et al., 2022). The system was positioned within a cubic simulation box, and a disulfide bridge formation between CYS 262 and CYS 285 was configured. The force field employed for these simulations was OPLS-AA/M (Robertson et al., 2015). We opted to perform serial minimization steps to ensure an optimal starting configuration. The first minimization step was a vacuum minimization utilizing the Steepest Descent (SD) algorithm, followed by a series of minimization steps in water. The solvation process employed the TIP3P water model and Na^+ and Cl^- ions in a concentration of 0.15 M. The second minimization step occurred treating the non-bonded interactions with a Cut-off and the SD algorithm; the third minimization step used Particle Mesh Ewald (PME) for long-range interactions and; the final minimization step employed PME in combination with the Conjugate Gradient algorithm.

We use the 100 resulting frames from the 100 ns simulation to select the best protein-ligand interaction. Performing catalytic center RMSD, we select the most divergent structures. We use π-stacking and distance analysis to decide the best catalytic triad (Ser153-His230-Asp-198) coordination with PET. With the elected structure, we performed a new Docking following the conditions above. This process created a protein-ligand complex, forming the foundation for subsequent MD simulations.

We ran a 100 ns simulation for the ensemble docking and extracted one structure per nanosecond. Next, we calculated the Root Mean Square Deviation (RMSD) of the catalytic center, including all the residues described as relevant for the substrate accommodation, and selected the ones presenting the higher values of RMSD. We submitted each structure for molecular docking and filtered them by the number and types of interactions, proximity to the catalytic residues, and the final configuration pose of PET, based on the *Is*PETase literature. The selected structure was used to generate the protein-ligand complex for the starting point of subsequent Molecular Dynamics (MD) simulations.

2.3. Molecular dynamics simulations

In this phase, we assembled the simulations in two distinct systems: one dedicated to elucidating the behavior of the free esterase, denoted as $PET30_F$, and the other involving the PET trimer bound at the binding pocket, referred to as $PET30_B$.

We selected the OPLS-AA/M FF and used the water molecules TIP4P model. We added Na^+ and Cl^- ions to maintain a neutralized system, mimicking a physiological condition of 0.15 M. An additional energy minimization step was executed, employing the Steepest Descent algorithm. The LINCS (Linear Constraint Solver) algorithm was utilized to constrain covalent bond lengths during the equilibration phase. In the NVT ensemble, the V-rescale thermostat heated the system to 300 K over 1 ns. Subsequently, in the NPT ensemble equilibration, the Parrinello-Rahman barostat maintained a pressure of 1 bar over 1 ns. Finally, the production step was performed for 1 μs simulation. Each system underwent five replicas of simulations, giving a total of 10 μs. Essential analyses were conducted, such as RMSD, Root Mean Square Fluctuation (RMSF), Radius of Gyration (R_g), Solvent Accessible Surface Areas (SASA), hydrogen bond analysis (HB), and Dictionary of Secondary Structure of the Protein (DSSP). The Supplementary Material contains information regarding the details of general trajectory analyses.

2.4. Principal component analysis and free energy profile

A multi-step process was executed to conduct Principal Component Analysis (PCA). We used the trajectories of the five replicas of each system separately, removing rotational and translational motions from the trajectories. Employing the `Covar` module in Gromacs, a covariance matrix was systematically generated based on the Cartesian coordinates of the protein backbone atoms over the trajectory. The obtained covariance matrix was then subjected to eigenvalue-eigenvector analysis using the `Anaeig` module. This analytical step identifies the principal components (PCs) of motion inherent in the system. We projected the entire simulation trajectory onto the identified principal components using the trajectory and the calculated eigenvectors. To construct the Free Energy Profile, we used the MD-Davis Python library (Maity and Pal, 2022) with PC1 and PC2 as input.

3. Results and discussion

The decision to model the initial 27 residues segment was driven by the acknowledgment of the limitations in available structural information, the potential impact of the missing segment on overall dynamics, and the pragmatic choice to adhere to evolutionarily selected sequences for a comprehensive exploration of PET30's behavior in MD simulations. This strategy was critical for a more nuanced understanding of the protein's structural dynamics and functional implications.

Both systems, $PET30_F$, and $PET30_B$, were simulated in quintuplicate to avoid drawing conclusions based on low-probability events due to specific local minima captured by one single trajectory (Knapp et al., 2018). Each replica composing the energy landscape associated with the global movement of PET30 systems can be considered equally relevant. However, each one depicts a different ensemble of local minima. This way, we must be careful when drawing conclusions based on the average of the five replicas or if the analysis requires consideration of specific energy minima, i.e., analyzing the event occurring in each replica separately.

Moreover, we take into consideration the effect of the molecular docking method. Docking estimates the binding pose between the protein and the ligand. However, the protein remains rigid during the docking process. Since there is no structure of PET30 co-crystallized with PET, we know that our initial $PET30_B$ system is an approximation. Employing molecular docking to generate an initial protein-ligand complex structure for MD simulations justifies the difficulty of the system achieving an optimal conformation of interaction. Thus, we observe different $PET30_B$ replicas exploring distinct levels of interaction with PET. Replica 1 shows the PET ligand leaving the binding pocket but eventually returning; replicas 2 and 5 show the ligand eventually leaving and staying out, interacting with a different portion of the protein and; replicas 3 and 4 keep the ligand tightly bound at the binding pocket throughout the whole simulation **SFig.**13,20-22.

3.1. Structural profiling of PET30: insights and comparison with IsPETase

The whole structure of PET30 comprises 366 residues in total. However, PDB 7PZJ missed the initial 27 residues and the C-terminal 300-366; thus, we performed a modeling step. Zhang et al. (Zhang et al., 2022) demonstrated at a web lab that PET30 keeps its catalytic activity unaltered even after removing residues 300 to 366 (called PET30ΔPorC in their work); thus, we removed the final modeled segment and kept the first 27 residues (validation results found in **SFig.**1-4). Comparing the structure of our model with *Is*PETase (PDB 6EQE (Austin et al., 2018)), the superposition is notable, and the structure's alignment results in a 0.735 RMSD value **Fig. 2**A.

*Is*PETase has a core β-sheet composed of 9 β-strands (β1-β9), surrounded by 7 distinct α-helix (α1-α7) and loops connecting each secondary structure element. PET30's β-sheet core exhibits an extra β-strand close to the C-terminal end, labeled as β10 **Fig. 2**B. Two additional helices appeared after we modeled the initial segment of PET30,
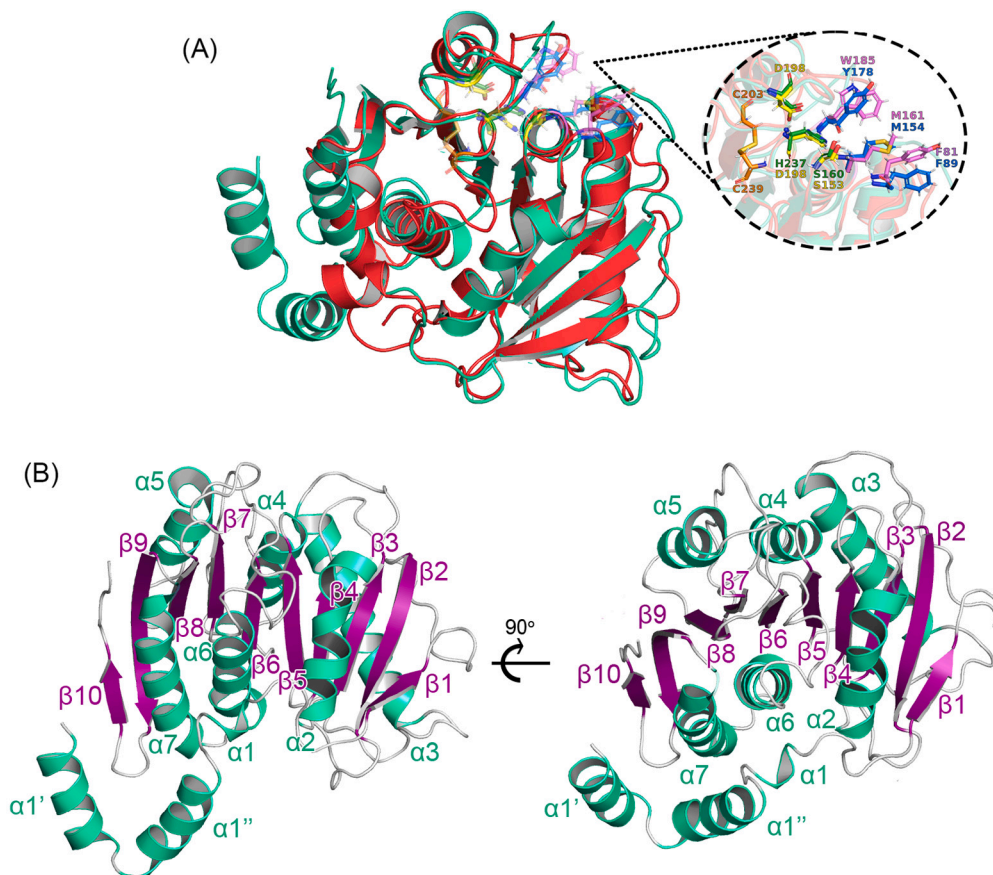
Fig. 2. A) Structure of PET30 model (green cyan) aligned to *Is*PETase structure (red). The catalytic residues of PET30 (Ser153, Asp198, His230) colored in yellow, and *Is*PETase represented (Ser160, Asp206, and His237) in green; auxiliary residues of PET30 (Phe80, Met154, and Tyr178) depicted in blue, and auxiliary residues from *Is*PETase (Tyr81, Met161, and Trp185) marked as pink. A disulfide bridge (only present in the *Is*PETase) is illustrated as orange. B) Structure of the PET30 model, depicting each secondary structure individually. Pet 30 core has a β-sheet composed of ten β-strands, named β1 to β10 from the N-terminal end; and nine α-helices, naming α1' and α1' the modeled helices, and α1 to α7 the correspondent helices with *Is*PETase structure.

which we called α1' and α2". This naming choice is based on two considerations. First, considering these helices come before the canonical ones, we wanted to keep the original numbering of α1 to α7. Additionally, MD results demonstrate that these helices are not stable. DSSP analysis shows that α1', composed of residues 2-13, quickly turns into coil structure; α1", comprising residues 15-27, reduces its helix structure size, with residues 15-18 and 25-27 presenting as a coil for 85% of the time; whereas residues 19-24 keeps it helical structure for over 60% of the time.

Furthermore, a comparison between PET30 and *Is*PETase structures reveals key distinguished features. First, *Is*PETase exhibits two disulfide bridges (Han et al., 2017), while PET30 is described only with one. The extra bridge of *Is*PETase connects two loops that harbor the catalytic residues Asp and His, guaranteeing that they do not get too far apart. In the position where the analogous Cys residues should be, we find a Gly and a Val instead. In this sense, we measured the distance between Gly195 and Val232 over time. Disulfide bonds typically have a length of 2.05 Å, with 3.0 Å being used as the PDB database's cutoff for disulfides (Sun et al., 2017). From our simulations, we observed that the PET30$_F$ Gly195-Val232 distance starts at 3.0 Å apart, but this distance varies, sometimes increasing until 5.0 Å. For PET30$_B$, the distance is even more prominent, starting at 3.0 Å and reaching 6.0 Å around 300 ns, staying at this distance for almost all the simulation **Fig. 3**D. From these insights, it can be inferred that the absence of the expected disulfide bridge in PET30 introduces greater flexibility and variability in the Gly195-Val232 distance, potentially influencing the enzyme's catalytic efficiency in PET degradation. Since the presence of the PET molecule further increases the distance between the residues, it is reasonable to

assume that the amount of stress over the loop by the presence of the ligand affects the PET30 catalytic process. This structural distinction offers a plausible explanation for the observed differences in catalytic performance between PET30 and *Is*PETase. It indicates the importance of the disulfide bridge in modulating enzymatic activity in the context of PET degradation.

One notable structural feature is a conserved string of four Gly residues composing the initial segment of the helix α4 (Gly155-Gly156-Gly157-Gly158), also present in the *Is*PETase. Furthermore, PET30 has an additional four Gly-residues motif at the initial segment of the helix α6 (Gly238-Gly239-Gly240-Gly241). Given that Gly residues' lack of side-chain provides them with increased flexibility, they tend to decrease helix stability. This decrease in helix stability occurs because Gly residues are, in fact, so flexible that the entropy effect accentuates enough to drive the structural change from a defined secondary structure to a loop (Imai and Mitaku, 2005). Surprisingly, DSSP analysis reveals that (Gly)$_4\alpha$4 stays as a helix 100% of the time. Diversely, three out of 4 Gly residues in the helix α6 remain as helix for about 35% of the time, and the rest show coil behavior.

Another divergence arises when comparing the binding site of PET30 and *Is*PETase. While *Is*PETase's binding motif involves Tyr87-Met161-Trp185 (Tyr-Met-Trp), PET30 substitutes two residues, adopting Phe80-Met154-Tyr178 (Phe-Met-Tyr) as its auxiliary residues. Intriguingly, a mutational study of PET30 has illuminated the critical role of specific residues in its catalytic function. Mutants PET30(Phe80Tyr) and PET30(Tyr178Trp), as well as a variant featuring both mutations, exhibited a loss of activity in degrading PET. These findings highlight the delicate interplay between the binding motif and catalytic activity
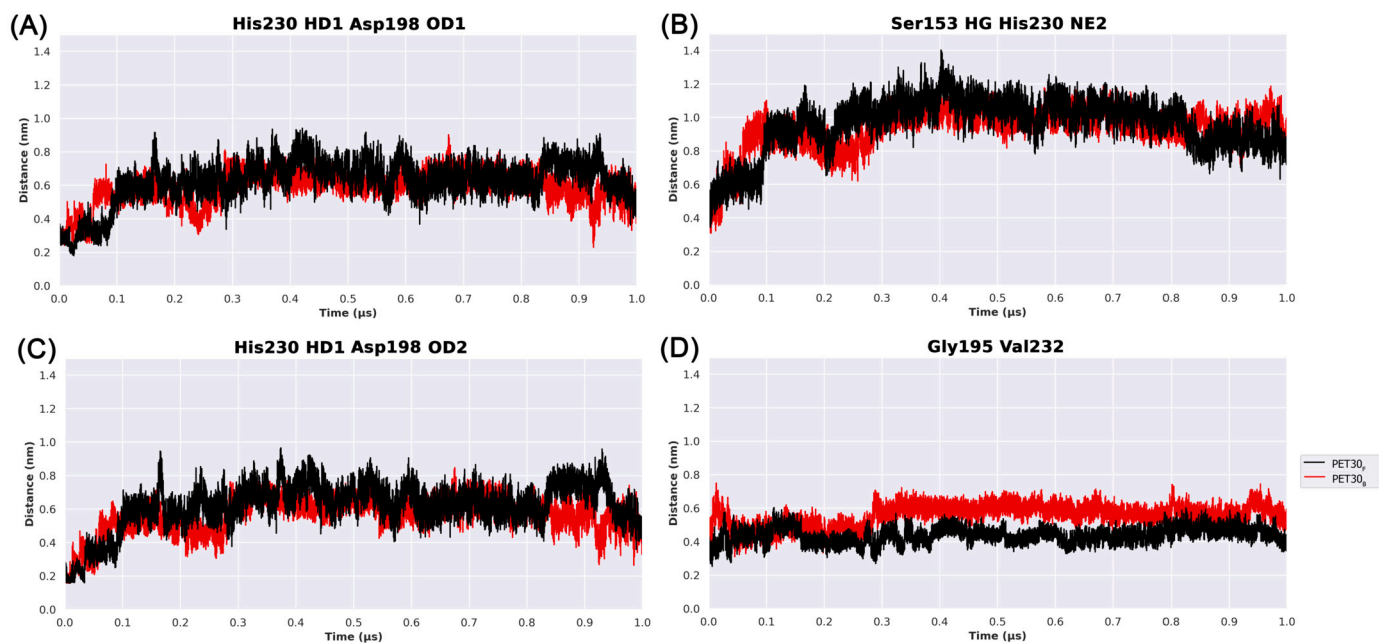
Fig. 3. Measurement of the distance between significant residues over time. The PET30$_F$ represented in color black and PET30$_B$ depicted in red A) Distance between hydrogen atom HD1 from His230 and the oxygen atom OD1 from Asp198. B) Distance between hydrogen atom HG from Ser153 and the nitrogen ϵ atom from His230. C) Distance between hydrogen atom HD1 from His230 and the oxygen atom OD2 from Asp198. D) Minimal distance between residues Gly195 and Val232, where the *Is*PETase structure has an extra disulfide bridge.

in PET-degrading enzymes, emphasizing the intricate relationship between sequence, structure, and function in these significant proteins. The role of the auxiliary residues in PET30 will be discussed in more depth later.

3.2. The halting of the catalytic triad: when it is time to hold their ground

As shown in **Fig. 1**C, the enzyme-substrate complex should have a specific residue coordination. The hydrogen from Nδ of His230 pairs with the oxygen from the Asp198 residue; the hydrogen belonging to the hydroxyl group of Ser153 aligns with the Nϵ of His230 and; the oxygen from the hydroxyl group of Ser153 interacts with a carbon from the ester group of the substrate molecule. In this sense, we assessed the distance among these groups throughout the simulations.

In the presence of the PET molecule, there is a notable reduction in the distance between the hydrogen bonded to the nitrogen delta (Nδ) of His230 and the oxygens from Asp198, suggesting a coordinated interaction **Fig. 3**A,C. Additionally, the hydrogen from the Ser153 hydroxyl group consistently maintains closer proximity to the nitrogen epsilon (Nϵ) of His230 in PET30$_B$ compared to PET30$_F$, providing further evidence of coordination among catalytic residues **Fig. 3**B. Although the distance between Ser153 and the PET molecule remains relatively constant across replicas 3 and 4, their distances vary from the PET center of mass **SFig.**27. Examination of the dihedral distribution of Ser153 **SFig.**23 reveals a flipping behavior concurrent with shifts of the PET molecule within the binding pocket.

Furthermore, RMSD (**Fig. 4**A) and RMSF (**Fig. 4**E) demonstrate a slightly increased overall backbone position variation relative to the initial structure and flexibility for PET30$_B$. However, the catalytic residues situated in specific regions of the protein either do not change their degree of flexibility compared to PET30$_F$ or even become less flexible in the presence of PET. Moreover, we measured the distance between the catalytic residues. This result is consistent with previous observations from *Is*PETase. Studies of *Is*PETase demonstrate the importance of certain regions becoming more flexible while retaining the rigidity of other regions to maintain catalytic efficiency, such as the flexibility of Ser214 and Trp185, demonstrated by Liu et al. (2022). They showed

that Ser214 provides a minor steric hindrance, giving more flexibility at the Trp185 site of isPETase, which is beneficial to the wobbling of the Trp185 site and stable binding to the PET aromatic ring. For PET30, the analogous residues by alignment are His206, respective to Ser214, and Tyr178, respective to Trp185. Zhang et al. (2022) tested the mutation Ser214His and observed that while it improved thermostability, it also decreased the catalytic efficiency, suggesting that this could be a potential mutation to improve PET30 efficiency. The implication of the interaction with Tyr178, one of the auxiliary residues, will be discussed next.

3.3. The role of the auxiliary residues: the sidekicks step into the spotlight

Our simulation reveals a significant feature of the auxiliary residues during the interaction between PET30 and PET. ΔRMSF (**Fig. 4**E) reveals that the catalytic triad residues lessen their flexibility, and the three auxiliary residues become more rigid - or at least keep the same level of flexibility of PET30$_F$ - despite the slight overall shifting of RMSF towards higher flexibility. This observation suggests that these residues attain some level of coordination. To investigate this mechanism further, we observed the distances of Phe80-Met154, Phe80-Tyr178, and Met154-Tyr178 and their distance to the PET molecule.

Distinct differences between PET30$_F$ and PET30$_B$ emerge when considering simulations where the PET molecule remains tightly bound to the binding pocket and those where it detaches. In PET30$_F$ replicas and replicas 1, 2, and 5 of PET30$_B$ (where PET detaches briefly), the distance between Phe80 and Tyr178 exhibits considerable variation over time. In contrast, replicas 3 and 4 of PET30$_B$ maintain a consistently close distance of approximately 6 Å throughout the entire simulation. Upon closer examination of PET30$_B$ replicas 3 and 4 and their interaction with each auxiliary residue and PET, it becomes evident that Phe80 and Tyr178 maintain a more stable distance from PET than Met154. This observation might be because Phe80 and Tyr174 can interact with PET through π-π stacking.

Furthermore, DSSP analysis **SFig.**9 indicates that Phe80 and Tyr178 remain closely associated in the presence of PET despite adopting a coil conformation. This observation indicates the PET molecule's influence in coordinating these residues, as evidenced by their distinctive
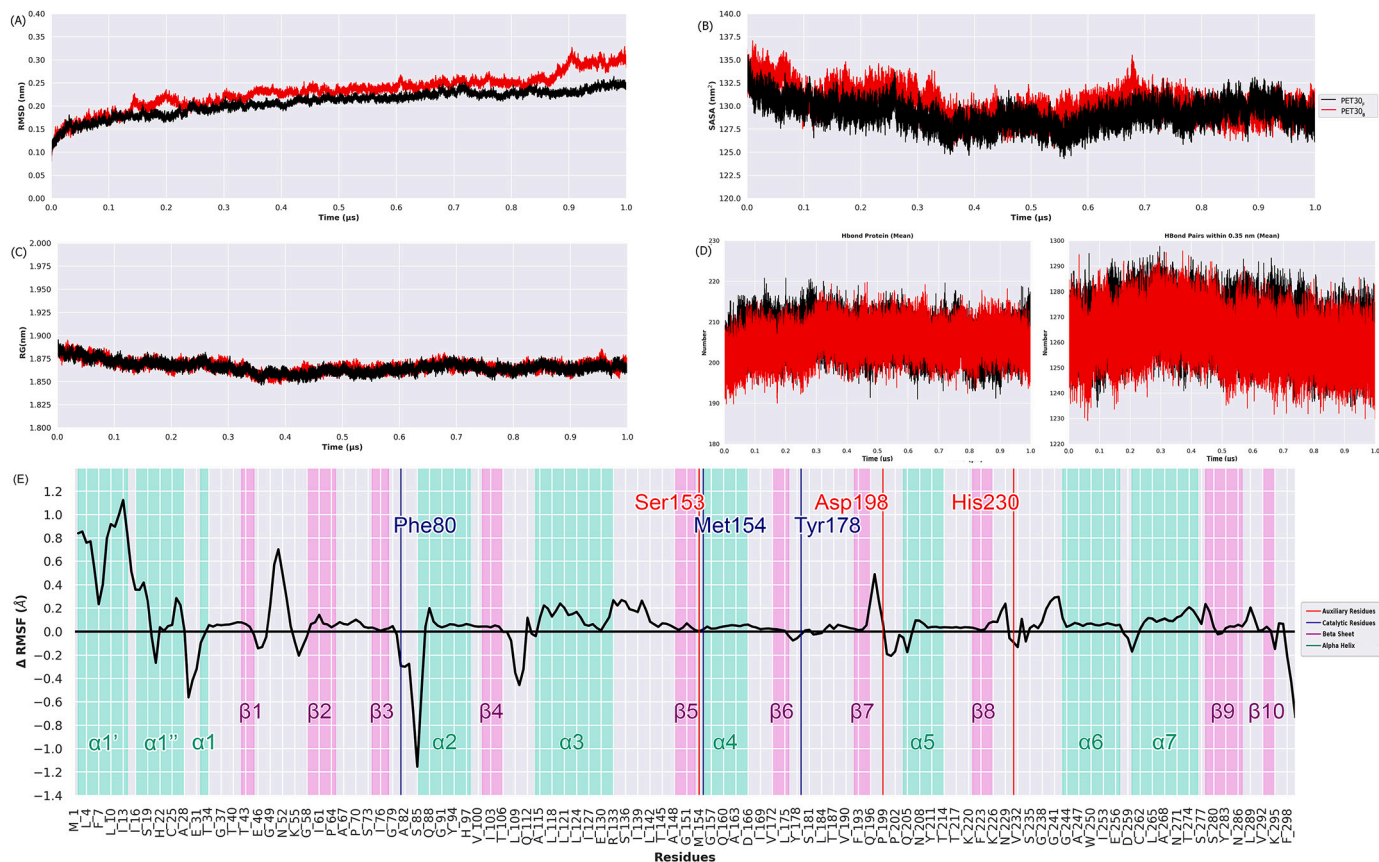
Fig. 4. MD trajectory analyses. The PET30$_F$ is represented in black, and the PET30$_B$ is depicted in red. Each graph characterizes the average result of the five replicas. A) RMSD result. B) SASA result. C) Rg result. D) HB results. On the left, the graph considers the distance of 0.35 nm and the angle of 30°; on the right, the graph considers only the distance of 0.35 nm. E) ΔRMSF result. ΔRMSF is calculated as RMSF PET30$_B$ - RMSF PET30$_F$. Positive values indicate higher flexibility of the PET30$_B$ whereas negative values reveal higher flexibility of PET30$_F$. The regions representing the β-strands are colored in cyan, and the regions indicating the α-helices are colored in violet. The red lines indicate the catalytic residues and the dark blue lines indicate the auxiliary residues.

behavior. Additionally, despite being in a coil conformation, Phe80 and Tyr178 tend to hold together when interacting with PET. This observation further underscores the coordinating effect of the PET molecule on these auxiliary residues.

3.4. Taking the wrong avenue: when the PET molecule gets lost around the protein

The initially available PET30 structure exhibited a catalytic pocket conformation unsuitable for binding, as demonstrated by incongruent results from molecular docking compared to literature expectations Tournier et al. (2020) (see Supplementary Materials). Then, ensemble docking was employed to generate PET30 structures more aligned with the anticipated binding conformation. Poses exhibiting characteristics such as an open pocket and proper alignment of catalytic and auxiliary residues were selectively chosen. Comparative analysis of various docking results utilizing different PET30 conformations revealed a more suitable outcome than the initial docking attempt with the native PDB structure. Notably, discrepancies in the alignment of catalytic residues, especially coordination of the catalytic residues, in the original structure were rectified in the final structure, demonstrating correct alignment and optimal distance. The selected docking result was then utilized in our MD simulations, exhibiting the PET molecule adopting an optimal conformation within the catalytic pocket. These simulations confirmed the efficacy of the refined approach in capturing the biologically relevant enzyme-substrate binding conformation within a short timeframe.

Our first concern was how long the PET molecule would stay in contact with the binding site **SFig.**27. Since our simulations reach the

microsecond scale, an unbinding event is expected. Generally, residence time varies from picoseconds to milliseconds (Huang and Caflisch, 2011), and the PET30 binding site is entirely external to the protein structure, composing a shallow pocket. From our simulations, we observed the unbinding of PET in 2 out of 5 replicas, which we kept to calculate the averages of each analysis. Replica 2 shows the unbinding occurring around 300 ns, where PET leaves the binding pocket, circles the protein, and lodges in a pocket close to the N- and C-termini junctions. Replica 5 shows the first unbinding event occurring around 270 ns, and the PET molecule relocates a few angstroms away from the binding pocket but returns to the binding pocket around 300 ns. Later, the PET leaves again, around 400 ns. Here, we note that close to the binding pocket, a helix, formed by residues 180-185, and an adjacent coil, consisting of residues 205-212, are arranged into a road-like pattern, where the PET molecule starts trailing. Most of these residues are polar, and only two are aromatic (His206 and His210); we notice that Tyr211 is aromatic, but it is the only residue in the helix that keeps interacting with the inside residues of the protein, never flipping to interact with the PET molecule. The PET molecule slowly crawls from the binding pocket until it starts interacting with the last residues of this sideway avenue. However, around 470 ns, it starts moving backward and stops at a position interacting with the initial residues from the road (180-182 from the coils and 205-212 from the helix) (Supplementary Material Movie-PET30B5). Replica 1 also shows an unbinding around 50 ns, but the PET molecules return to the binding pocket at 300 ns and stay there until the end of the simulation. Replicas 3 and 4 maintain the PET molecule tightly bound close to the catalytic site all the time.

3.5. Simulations aftermath: contrasting PET30$_F$ and PET30$_B$ dynamics

Next, we will highlight the main observations distinguishing PET30$_F$ and PET30$_B$. RMSD analysis (**Fig. 4**A) revealed that PET30$_B$ exhibits a slightly higher overall backbone position variation than PET30$_F$, particularly after 100 ns, reaching a significant difference of 0.5 nm at approximately 900 ns. This observation suggests that the presence of PET introduces a subtle yet cumulative effect on the structure dynamics of PET30.

Moreover, ΔRMSF analysis (**Fig. 4**E) indicate nuanced differences in the flexibility of PET30$_F$ and PET30$_B$. While the overall ΔRMSF difference is minimal (approximately 0.1 nm), certain regions crucial for the catalytic mechanism exhibited significant variations. Notably, the catalytic triad residues (Ser153, Asp198, and His230) showed distinct flexibility patterns, indicating the influence of PET binding on their dynamics.

In the modeled segment (residues 1 to 27), PET30$_B$ displayed higher flexibility, particularly around residue 21, showcasing a significant contrast of 1.3 nm compared to PET30$_F$. Interestingly, the auxiliary residue Phe80 region exhibited a marked decrease in flexibility in PET30$_B$, suggesting a potential role in ligand accommodation. Regions surrounding catalytic residues displayed consistent flexibility, emphasizing the intricate interplay between ligand binding and enzymatic function.

DSSP analysis unveils distinct secondary structure variations between PET30$_F$ and PET30$_B$ systems (see **SFig.**9). Specifically, in β-strand 3 (residues 219-228), the last four residues (225-228) exhibit fluctuating conformations between coil and β-sheet throughout the simulation. PET30$_B$ maintains a more prolonged β-sheet conformation in this segment than PET30$_F$. Also, residues 229-233, including the catalytic residue His230, alternate between α-helix and coil conformations. PET30$_B$ consistently favors the α-helix conformation, which is more extended than PET30$_F$ in this region. Furthermore, DSSP analysis reveals a structural difference in residue 288, forming a β-turn between β-strands β9 and β10. In the presence of the ligand, this residue adopts a coil conformation exclusively, contrasting with PET30$_F$, where it sporadically assumes a β-sheet conformation. This observation aligns with the dRMSF results, indicating reduced flexibility in the absence of the ligand. Residues 226-228, forming a loop between β-strand β8 and helix α6, exhibit a β-strand conformation more frequently (25% of the time) in the presence of the PET molecule, compared to the free enzyme state (15% of the time). The flexibility analysis of residue 152, adjacent to the catalytic Ser153, shows a balanced distribution between helix, β-sheet, and coil conformations, consistent across both PET30$_F$ and PET30$_B$. Notably, the helix α2 (residues 83-96) displays dynamic variations over time, with residue 83 evenly splitting between helix and coil, residues 84-88 favoring helix (55% of the time), residues 89-94 consistently adopting a helix conformation, residue 95 displaying a 75% helix conformation, and residue 96 favoring a coil conformation (90% of the time).

Furthermore, PCA revealed substantial distinctions between the PET30$_F$ and PET30$_B$ systems **Fig. 5**A,B. While the initial positions of each replica were nearly identical, with minor differences arising during equilibration, a noticeable divergence in energy distribution became evident. Each replica portrayed a unique distribution, and our analyses depicted two distinct pieces of information: clusters formed by the trajectory of each replica and clusters formed by the density of points.

The PC1 vs PC2 plot for PET30$_F$ displayed a more continuous landscape, suggesting that the enzyme fluctuates more freely among energy minima when unbound. In contrast, the PC1 vs PC2 plot for PET30$_B$ exhibited a more distinctive cluster, with some clusters entirely isolated from others. These findings indicate that the enzyme adopts specific conformations during interaction with the PET molecule. A comparison of the density plots revealed that PET30$_B$ had a higher density at specific points, while PET30$_F$ exhibited lower density with more distributed points. Notably, points from replicas 2 and 5 in PET30$_B$ remained closer to the initial position. Furthermore, looking into the

movies showing the principal movements captured in PCA of PET30$_F$ and PET30$_B$ (Supplementary material Movie-PCA-PET30$_F$ and Movie-PET30$_B$), we observe that when the PET molecule is present, the catalytic residues Ser152 and Asp198 hold their position close together. At the same time, His230 moves, closing its distance to the other catalytic residues, indicating increased coordination among them. On the other hand, in the absence of PET, the residues Asp198 and His230 fluctuate more, suggesting a lower level of coordination compared to PET30$_B$.

In the context of the free energy profile generated from the probability distributions of PC1 and PC2, a significant difference emerged between PET30$_F$ and PET30$_B$. The global minimum energy for PET30$_F$ was -17.1 kJ/mol, whereas PET30$_B$ reached -19.2 kJ/mol, indicating a difference of 2.1 kJ/mol. Furthermore, PET30$_B$ exhibited four well-separated small clusters, each reaching approximately -15 kJ/mol. In contrast, PET30$_F$ displayed a more scattered energy distribution, featuring one large cluster at -10 kJ/mol, four clusters within the larger one reaching -11 kJ/mol, and three smaller clusters reaching -14 kJ/mol, where one of them contains the global minimum cluster.

The outcomes obtained from the R$_g$ analysis (**Fig. 4**C) demonstrate a consistent similarity between PET30$_F$ and PET30$_B$, indicating virtually identical values. Both systems exhibit a slight compaction trend throughout the simulation. In the context of hydrogen bond analysis, it is observed that both PET30$_F$ and PET30$_B$ maintain a comparable number of internal hydrogen bonds (**Fig. 4**D), with these numbers exhibiting no significant variation throughout the simulation. SASA analysis (**Fig. 4**B) reveals a marginal increase in the overall surface area of the protein when interacting with the PET molecule. Notably, around the 800 ns mark, the SASA values for PET30$_F$ and PET30$_B$ converge, suggesting a comparable surface area in the simulation. These findings collectively suggest that the structural behavior variation between PET30$_F$ and PET30$_B$ is nuanced, and importantly, the presence of PET does not exert an abrasive impact on this enzyme.

4. Conclusions

PET30, identified as an esterase, exhibits activity in degrading PET, albeit with a lower catalytic efficiency than *Is*PETase. Nevertheless, our MD investigation reveals a favorable interaction between PET30 and PET. Furthermore, studying an enzyme with reduced catalytic efficiency provides a unique perspective on the evolution of plastic-degrading enzymes, shedding light on the ongoing process of adaptation toward PET degradation. The comparatively lower catalytic efficiency of PET30 signifies a stage in its evolutionary trajectory, suggesting that this enzyme is still fine-tuning its mechanisms for optimal PET degradation. This perspective contributes to our understanding of the dynamic nature of enzyme evolution in the context of plastic degradation, paving the way for future endeavors in designing more robust and efficient biocatalysts for addressing environmental challenges posed by synthetic polymers.

In conclusion, our findings demonstrate the intricate interplay between PET30 and PET, providing a molecular-level understanding of how the enzyme responds to and interacts with its substrate. These insights contribute valuable knowledge for the rational design of enzymes with enhanced PET-degrading capabilities, thereby advancing efforts in combating plastic pollution.

Declaration of competing interest

The authors declare that they have no known competing financial interests or personal relationships that could have appeared to influence the work reported in this paper.

Data availability

No data was used for the research described in the article.
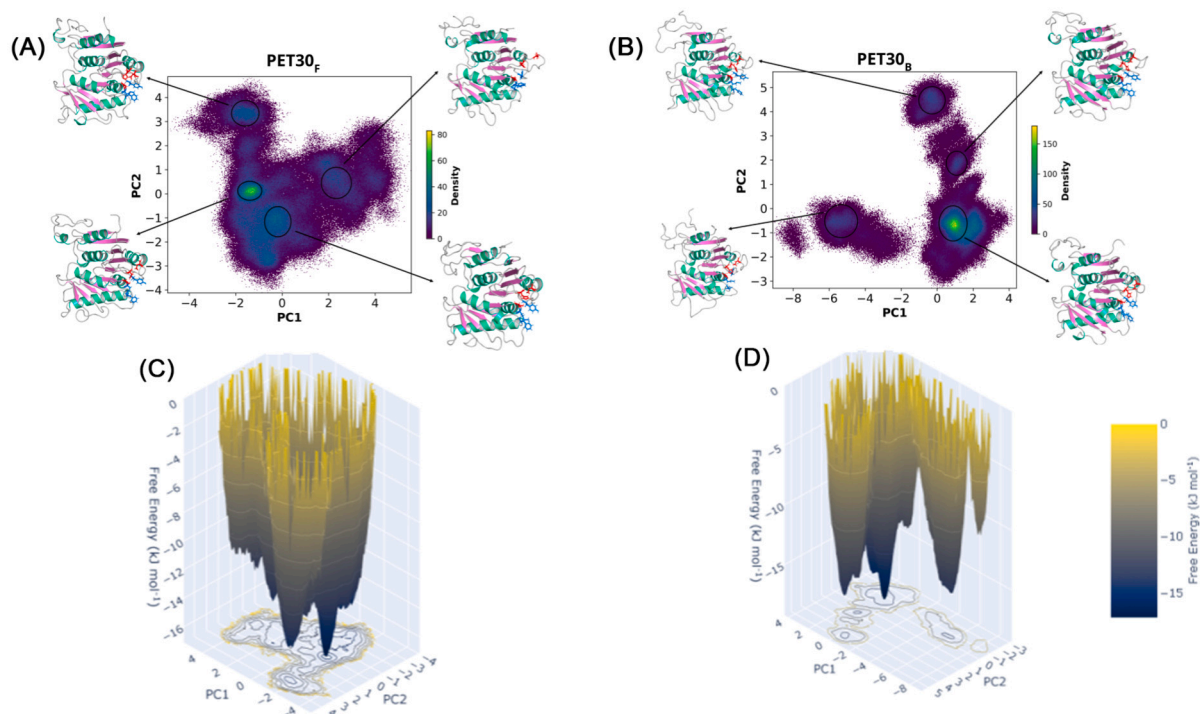
Fig. 5. PCA and energy profile. A) 2D plot of PCA from PET30$_F$, depicting PC1 in the x-axis and PC2 in the y-axis, colored by the density of points. Structures of the four most representative clusters are shown. B) 2D plot of PCA from PET30$_B$, depicting PC1 in the x-axis and PC2 in the y-axis, colored by the density of points. Structures of the four most representative clusters are shown. C) Free energy profile derived from PET30$_F$ PCA. D) Free energy profile derived from PET30$_B$ PCA.

Acknowledgement

Appendix A. Supplementary material

Supplementary material related to this article can be found online at https://doi.org/10.1016/j.crstbi.2024.100130.

References

Allouzi, M.M.A., Tang, D.Y.Y., Chew, K.W., Rinklebe, J., Bolan, N., Allouzi, S.M.A., Show, P.L., 2021. Micro (nano) plastic pollution: the ecological influence on soil-plant system and human health. Sci. Total Environ. 788, 147815.

Austin, H.P., Allen, M.D., Donohoe, B.S., Rorrer, N.A., Kearns, F.L., Silveira, R.L., Pollard, B.C., Dominick, G., Duman, R., El Omari, K., et al., 2018. Characterization and engineering of a plastic-degrading aromatic polyesterase. Proc. Natl. Acad. Sci. 115, E4350–E4357.

Berman, H.M., Westbrook, J., Feng, Z., Gilliland, G., Bhat, T.N., Weissig, H., Shindyalov, I.N., Bourne, P.E., 2000. The protein data bank. Nucleic Acids Res. 28, 235–242.

Bowie, J.U., Lüthy, R., Eisenberg, D., 1991. A method to identify protein sequences that fold into a known three-dimensional structure. Science 253, 164–170.

Carr, S.A., Liu, J., Tesoro, A.G., 2016. Transport and fate of microplastic particles in wastewater treatment plants. Water Res. 91, 174–182.

Chen, K., Hu, Y., Dong, X., Sun, Y., 2021. Molecular insights into the enhanced performance of ekylated petase toward pet degradation. ACS Catal. 11, 7358–7370.

Childers, M.C., Daggett, V., 2017. Insights from molecular dynamics simulations for computational protein design. Mol. Syst. Des. Eng. 2, 9–33.

Colovos, C., Yeates, T.O., 1993. Verification of protein structures: patterns of nonbonded atomic interactions. Protein Sci. 2, 1511–1519.

Csizmadia, P., 1999. Marvinsketch and Marvinview: molecule applets for the world wide web. In: Proc. of ECSOC-3, the 3rd Int Electr Conf on Synthetic Organic Chem, September 1–30, p. 367a369.

Cui, Y., Chen, Y., Liu, X., Dong, S., Tian, Y., Qiao, Y., Mitra, R., Han, J., Li, C., Han, X., et al., 2021. Computational redesign of a petase for plastic biodegradation under ambient condition by the grape strategy. ACS Catal. 11, 1340–1350.

Dodda, L.S., Cabeza de Vaca, I., Tirado-Rives, J., Jorgensen, W.L., 2017a. Ligpargen web server: an automatic opls-aa parameter generator for organic ligands. Nucleic Acids Res. 45, W331–W336.

Dodda, L.S., Vilseck, J.Z., Tirado-Rives, J., Jorgensen, W.L., 2017b. 1.14* cm1a-lbcc: localized bond-charge corrected cm1a charges for condensed-phase simulations. J. Phys. Chem. B 121, 3864–3870.

Eberhardt, J., Santos-Martins, D., Tillack, A.F., Forli, S., 2021. Autodock vina 1.2. 0: new docking methods, expanded force field, and python bindings. J. Chem. Inf. Model. 61, 3891–3898.

Egmond, M.R., de Vlieg, J., 2000. Fusarium solani pisi cutinase. Biochimie 82, 1015–1021.

Fecker, T., Galaz-Davison, P., Engelberger, F., Narui, Y., Sotomayor, M., Parra, L.P., Ramírez-Sarmiento, C.A., 2018. Active site flexibility as a hallmark for efficient pet degradation by I. Sakaiensis petase. Biophys. J. 114, 1302–1312.

Han, X., Liu, W., Huang, J.W., Ma, J., Zheng, Y., Ko, T.P., Xu, L., Cheng, Y.S., Chen, C.C., Guo, R.T., 2017. Structural insight into catalytic mechanism of pet hydrolase. Nat. Commun. 8, 2106.

Hooft, R.W., Vriend, G., Sander, C., Abola, E.E., 1996. Errors in protein structures. Nature 381, 272.

Howard, S.A., McCarthy, R.R., 2023. Modulating biofilm can potentiate activity of novel plastic-degrading enzymes. NPJ Biofilms Microbiomes 9, 72.

Huang, D., Caflisch, A., 2011. The free energy landscape of small molecule unbinding. PLoS Comput. Biol. 7, e1002002.

Imai, K., Mitaku, S., 2005. Mechanisms of secondary structure breakers in soluble proteins. Biophysics 1, 55–65.

Joo, S., Cho, I.J., Seo, H., Son, H.F., Sagong, H.Y., Shin, T.J., Choi, S.Y., Lee, S.Y., Kim, K.J., 2018. Structural insight into molecular mechanism of poly (ethylene terephthalate) degradation. Nat. Commun. 9, 382.

Jorgensen, W.L., Tirado-Rives, J., 2005. Potential energy functions for atomic-level simulations of water and organic and biomolecular systems. Proc. Natl. Acad. Sci. 102, 6665–6670.

Kim, D.E., Chivian, D., Baker, D., 2004. Protein structure prediction and analysis using the robetta server. Nucleic Acids Res. 32, W526–W531.

Knapp, B., Ospina, L., Deane, C.M., 2018. Avoiding false positive conclusions in molecular simulation: the importance of replicas. J. Chem. Theory Comput. 14, 6127–6138.

Laskowski, R.A., MacArthur, M.W., Moss, D.S., Thornton, J.M., 1993. Procheck: a program to check the stereochemical quality of protein structures. J. Appl. Crystallogr. 26, 283–291.

Lindahl, Abraham, Hess, van der Spoel, 2022. Gromacs 2021.5. https://doi.org/10.5281/zenodo.5850051.

Liu, Y., Liu, Z., Guo, Z., Yan, T., Jin, C., Wu, J., 2022. Enhancement of the degradation capacity of ispetase for pet plastic degradation by protein engineering. Sci. Total Environ. 834, 154947.

Lüthy, R., Bowie, J.U., Eisenberg, D., 1992. Assessment of protein models with three-dimensional profiles. Nature 356, 83–85.

MacLeod, M., Arp, H.P.H., Tekman, M.B., Jahnke, A., 2021. The global threat from plastic pollution. Science 373, 61–65.

Maity, D., Pal, D., 2022. MD DaVis: interactive data visualization of protein molecular dynamics. Bioinformatics 38, 3299–3301.

Maurya, A., Bhattacharya, A., Khare, S.K., 2020. Enzymatic remediation of polyethylene terephthalate (pet)–based polymers for effective management of plastic wastes: an overview. Front. Bioeng. Biotechnol. 8, 602325.

Pontius, J., Richelle, J., Wodak, S.J., 1996. Deviations from standard atomic volumes as a quality measure for protein crystal structures. J. Mol. Biol. 264, 121–136.

Revel, M., Châtel, A., Mouneyrac, C., 2018. Micro (nano) plastics: a threat to human health? Curr. Opin. Environ. Sci. Health 1, 17–23.

Robertson, M.J., Tirado-Rives, J., Jorgensen, W.L., 2015. Improved peptide and protein torsional energetics with the opls-aa force field. J. Chem. Theory Comput. 11, 3499–3509.

Sanner, M.F., et al., 1999. Python: a programming language for software integration and development. J. Mol. Graph. Model. 17, 57–61.

Sharma, B., Dangi, A.K., Shukla, P., 2018. Contemporary enzyme based technologies for bioremediation: a review. J. Environ. Manag. 210, 10–22.

Son, H.F., Cho, I.J., Joo, S., Seo, H., Sagong, H.Y., Choi, S.Y., Lee, S.Y., Kim, K.J., 2019. Rational protein engineering of thermo-stable petase from ideonella sakaiensis for highly efficient pet degradation. ACS Catal. 9, 3519–3526.

Sun, M.a., Wang, Y., Zhang, Q., Xia, Y., Ge, W., Guo, D., 2017. Prediction of reversible disulfide based on features from local structural signatures. BMC Genomics 18, 1–10.

Tournier, V., Topham, C., Gilles, A., David, B., Folgoas, C., Moya-Leclair, E., Kamionka, E., Desrousseaux, M.L., Texier, H., Gavalda, S., et al., 2020. An engineered pet de-polymerase to break down and recycle plastic bottles. Nature 580, 216–219.

Trott, O., Olson, A.J., 2010. Autodock vina: improving the speed and accuracy of docking with a new scoring function, efficient optimization, and multithreading. J. Comput. Chem. 31, 455–461.

Williams, C.J., Headd, J.J., Moriarty, N.W., Prisant, M.G., Videau, L.L., Deis, L.N., Verma, V., Keedy, D.A., Hintze, B.J., Chen, V.B., et al., 2018. Molprobity: more and better reference data for improved all-atom structure validation. Protein Sci. 27, 293–315.

Yoshida, S., Hiraga, K., Takehana, T., Taniguchi, I., Yamaji, H., Maeda, Y., Toyohara, K., Miyamoto, K., Kimura, Y., Oda, K., 2016. A bacterium that degrades and assimilates poly (ethylene terephthalate). Science 351, 1196–1199.

Zhang, H., Perez-Garcia, P., Dierkes, R.F., Applegate, V., Schumacher, J., Chibani, C.M., Sternagel, S., Preuss, L., Weigert, S., Schmeisser, C., et al., 2022. The bacteroidetes ae-quorivita sp. and kaistella jeonii produce promiscuous esterases with pet-hydrolyzing activity. Front. Microbiol. 12, 803896.